Searching for Life in Hot Spring Carbonate Systems: Investigating Raman Spectra of Carotenoid-Bearing Organic Carbonaceous Inclusions from Travertines of Italy

A. E. O'Donnell[1]*, D. K. Muirhead[1], A. T. Brasier[1], E. Capezzuoli[2].

*[1]Department of Geology and Geophysics, School of Geosciences, University of Aberdeen, Aberdeen AB24 3UE, UK, [2]Department of Earth Sciences, University of Florence, Firenze, 50121, Italy, *Correspondence: a.odonnell.19@abdn.ac.uk*

Abstract

Carotenoid pigments provide some of the most common exclusively biogenic markers on Earth, and these organic pigments may be present in extra-terrestrial life. Raman spectroscopy can be used to identify carotenoids quickly and accurately through the inelastic scattering of laser light. In this study we show that Raman spectra of organic matter found in hot spring bacterial assemblages exhibit 'spectral overprinting' of the carotenoid spectrum by the carbon spectrum as the organic matter progressively breaks down. Here we present how, with increasing thermal maturity, the relative intensity of the carotenoid spectrum increases, and as maturity increases a low intensity carbon spectrum forms in the same region as the carotenoid spectrum. This carbon spectrum increases in intensity as the thermal maturity increases further, progressively obscuring the carotenoid spectrum until only the carbon spectrum can be observed. This means key carotenoid biogenic signatures in hot-spring deposits may be hidden within carbon spectra. A detailed study of the transition from carotenoid to carbon Raman spectra may help develop deconvolution processes that assist in positively identifying biogenic carbon over abiogenic carbon. Our results are relevant for the data analysis from the Raman spectroscopy instruments on the Perseverance (NASA) and Rosalind Franklin (ESA) rovers.

1. Introduction

Raman spectroscopy is a remotely deployable, non-destructive technique recently used in Martian exploration to analyze samples for organic compounds (Brolly et al., 2016; Chu, 2016; Ferralis et al., 2016; Hutchinson et al., 2014).

In this study Raman spectroscopy was used to identify unique spectra for carbon and carotenoid pigments within hot spring carbonate precipitates. We discuss how these spectra change due to spatial, temporal, and thermal variables within the Viterbo hot spring system.

1.1 Importance of Carotenoids and Carbon as biomarkers

Carotenoids are common pigment molecules found in a wide variety of plants, fungi and microorganisms on Earth (Maoka, 2020; Marshall and Marshall, 2010). They are used by these organisms to help absorb light for photosynthesis and to control molecular oxygen, or free radicals, produced during photosynthesis (Ma and Cui, 2022; Maoka, 2020). Carotenoids are geologically stable compounds that are detectable by Raman spectroscopy (Bowden and Taylor, 2019; French et al., 2015; Ma and Cui, 2022). Carotenoids on Earth are of exclusively biogenic origin, having no known abiogenic source (Baqué et al., 2020; Marshall and Marshall, 2010; Vítek et al., 2009). If these organic pigments are present in extra-terrestrial life, they would be a biomarker that could prove unequivocal biological origin of the host material.

Carbon is the main constituent of the carbonaceous material preserved in the geological record when biological organisms die and degrade. However carbon itself is not a direct biomarker as there are many sources of abiogenic carbon. When using Raman spectroscopy alone it is currently impossible to assign a biogenic or abiogenic source to the carbon (Pasteris and Wopenka, 2003).

We will show in this study how the carotenoid Raman spectrum and the carbon Raman spectrum change in biological samples of varying thermal maturity. This is relevant to determining if and how Raman spectra of carotenoids could be used to assign a biological origin to carbonaceous material, at and so could have an impact on approaches used in the search for life on Mars.

1.2 Raman Spectroscopy of Carbon

Raman spectroscopy of both amorphous and crystalline forms of carbonaceous material undergoing thermal maturation has been explored by others (e.g. Tuinstra and Koenig, 1970; Rouzaud et al*.*, 1983; Wopenka and Pasteris, 1993; Ferrari and Robertson, 2001; Beyssac et al., 2002; Busemann et al*.*, 2007; Muirhead et al., 2019). Much of this work has focused on the geological origin, thermal and burial history of the carbonaceous matter, examining how molecular structure affects the response of the carbon spectra (Beyssac et al., 2002; Chu, 2016; Kelemen & Fang, 2001; Wopenka, 1988). The Raman carbon spectrum refers to the disordered carbon and graphitic carbon ratio in the form of the D and G peaks. While the bulk material would be referred to as carbonaceous, the Raman spectrum of carbon refers to the molecular structure of the carbon alone, even if it is convoluted with other individual spectra (e.g. calcite and carotenoid) within the bulk spectrum. The ratio of disordered amorphous carbon to crystalline graphitic carbon, obtained through Raman spectra measurements, can be used as a geothermometry tool. This has been shown to work for temperatures up to 650°C (Beyssac et al., 2002). Above 650°C, all material will be composed of graphitic carbon, so no further changes can be identified until the carbon becomes diamond if there is sufficient temperature and pressure to do so, i.e. >4GPa and 950-1400°C (Cartigny et al., 2014; Shirey and Shigley, 2013). This technique has been successfully used to measure temperatures down to a low of 75°C (Muirhead et al., 2019). Lower temperatures (<100°C) are more challenging to investigate than higher temperatures (up to 650°C) as the Raman spectroscopy of carbon geothermometry technique has reduced sensitivity at low temperatures.

1.3 Raman Spectroscopy of Carotenoids

The National Aeronautics and Space Administration (NASA) and the European Space Agency (ESA) have designed miniaturized Raman spectroscopy experiments to identify compounds relevant to detecting life in situ on Mars. Current Raman systems on Mars have a detection sensitivity limit for organic compounds of around 1 part per million (ppm) (Razzell Hollis et al., 2021; Rull et al., 2017). Carotenoids have been demonstrated to be detectable by miniaturized Raman spectroscopy instruments at concentrations of 0.1ppm (Vítek et al., 2014). This shows that even trace amounts of carotenoid material could be detected on Mars if they were present.

Carotenoids are photosynthetic and photoprotective pigments that only biological processes can synthesise (Baqué et al., 2020; Marshall & Marshall, 2010; Vítek et al., 2009) and can be found in a wide variety of microorganisms including prokaryotes and eukaryotes (Jehlička et al., 2014; Takaichi & Mochimaru, 2007). There are more than 850 carotenoid structures currently known (Maoka, 2020; Marshall and Marshall, 2010), with some carotenoids, for example β-carotene, being very common across many groups of microorganisms. Other carotenoids such as salinixanthin are only found in a limited number of organisms (Jehlička et al., 2014; Takaichi & Mochimaru, 2007). Carotenoid compounds are thought of as geologically stable, with investigation into post-depositional diagenetic processes that may affect the carotenoid structure showing the detection of intact carotenoid compounds, fossilized 'perhydro' derivatives, or their diagenetic products to be possible (Marshall and Marshall, 2010). The depositional environment of the carotenoids can heavily influence the amount of preservation observed, with hypersaline and anoxic environments better for preservation than oxidising environments. (Killops and Killops, 2005; Lee and Brocks, 2011; Marshall and Marshall, 2010). Individual carotenoids exhibit varied diagenetic stability, with β-carotene having the lowest rates of diagenetic degradation (Killops and Killops, 2005). Intact carotenoids and their diagenetically altered products have been identified in sedimentary rocks and bitumen up to 1.6 Ga in age (Brocks et al., 2005; French et al., 2015; Lee and Brocks, 2011; Ma and Cui, 2022; Marshall and Marshall, 2010; Sinninghe Damsté and Koopmans, 1997; Vítek et al., 2014). Most experiments to date have used commercial laboratory extracted samples of carotenoids (Jehlička et al., 2014; Marshall & Marshall, 2010; Timlin et al., 2017), while few investigations have focussed on natural field samples (Jehlička & Oren, 2013).

1.4 Relevance and Application to Mars Research

Morphological features and bulk compositions obtained by remote and in situ detection, indicate that there is potential evidence for hot spring related silicic sinter (Gusev crater) and spring carbonate (Chryse Planitia) deposits on Mars (Komatsu & Brož, 2021; Linares & Rodríguez, 2013; Ruff et al., 2020; Ruff & Farmer, 2016). The terrestrial carbonate springs of Isona in the Pyrenean Tremp Basin (Linares and Rodríguez, 2013), and mud volcanoes (Komatsu and Brož, 2021), have been presented as analogous to circular features in the southern Chryse Planitia (Fig. 1). The Isona study postulates that contractional deformation led to perched aquifers along thrust faults within the Martian cryosphere, with fluids heated by regional magmatism (Linares and Rodríguez, 2013; Rodríguez et al., 2007). The release of these pressurized subsurface fluids led to the formation of surface lakes.

These hot spring travertines and sinters are an attractive target for Mars exploration because of the possible habitability of the liquid water (Baqué et al., 2020; Hays et al., 2017; McMahon et al., 2018) and the relatively high likelyhood that signs of life would be preserved by the mineral precipitation (McMahon et al., 2018).

1.5 Detectability of Carotenoids on Mars via Raman Spectroscopy

Carotenoid material has the capacity to be stable and preserved on Mars (Baqué et al., 2018). Carotenoids present a more stable biomarker than others such as DNA (Leuko et al., 2017). Experiments into the survivability of carotenoids in Mars analogue environments, on Earth and in Low Earth Orbit (LEO), have demonstrated that temperature oscillations, the Martian atmosphere and vacuum conditions had no effect on the compounds, with Ultra-Violet (UV) radiation degrading surface samples to the point where they would be undetectable within 1.5 million years (Baqué et al., 2020; Leuko et al., 2017), or perhaps 650 million years if in the top 4-5cm of the regolith (McMahon et al., 2018).

Solar radiation is seen as the most destructive factor for the preservation of carotenoid structures on the surface of Mars. However, based on results of analogue experiments mounted on the International Space Station (ISS), and in situ radiation measurements made by NASA's Curiosity rover at Gale Crater if the sample were buried within the Martian regolith at a depth of 2m, then the carotenoid signature in desiccated bacterial material might be detectable for > 13 million years(Baqué et al., 2020)). This means that future missions to Mars equipped with a drill such as found on the Rosalind Franklin (ESA) rover, could potentially detect carotenoid signatures in the subsurface.

2. Geological Setting of the Travertine Source Study Area

2.1 Travertines of Viterbo, Italy

Travertines are carbonate precipitates associated with terrestrial hot springs (Pedley, 1978). These hot springs provide a natural laboratory to study possible ancient Martian life-bearing analogue carbonate hot spring environments (Allen et al., 2000; Des Marais and Walter, 2019; Morris et al., 2010; Ruff and Farmer, 2016). Three actively precipitating travertine sites were here studied around Viterbo in Central Italy (Fig. 3a). The localities were Le Zitelle (42°25'34" N, 12°03'39" E, Elevation 291 meters above sea level (m.a.s.l.), Bullicame (42°25'13" N, 12°04'22" E, Elevation 297 m.a.s.l.), and Paliano (42°22'35" N, 12°03'26" E, Elevation 255 m.a.s.l.) (Fig. 3b). The springs are fed by meteoric waters collected from areas including the Cimini mountains and Lake Vico. These waters descend through the bedrock and are heated by regional volcanism during their deep circulation (maximum 2km depth), flowing through a confined carbonate reservoir under the Viterbo region (Piscopo et al., 2006; Della Porta et al., 2021). The waters are held in a sedimentary (carbonate and sulphate) reservoir by a low-permeability clay cap rock which thins out near Viterbo, allowing the carbonate saturated water to rise and reach the surface in that area (Piscopo et al., 2006).

When these waters surface, they de-gas and carbonates precipitate, with some springs depositing more than 1 mm of carbonate per day in the form of travertines (Folk, 1994, 1993; Piscopo et al., 2006). At the Le Zitelle sample locality, Pentecost and Coletta (2007) measured the $CaCO_3$ precipitation as a function of distance from the vent. They found a minimum precipitation rate of 13.4mg/cm^{-2} day^{-1} at 9.0m from the vent, and a maximum precipitation rate of 30.9 mg/cm^{-2} day^{-1} at 96.0m from the vent.

2.2 Microbial life

The hot springs of Viterbo host thriving microbial communities. Valeriani et al. (2018) studied the Bullicame hot spring, and found (via PCR metagenomics analysis) *Chloroflexi* and *Roseiflexus* bacteria, both in the water and microbial mat, with the bacterium *Thiofaba* common in the water but rare in the microbial mat. Many other genera of bacteria were found in lower percentages in the water, microbial mats, and the lithified travertine deposits. Cyanobacteria are common in both the microbial mats and in the lithified travertine deposits. It has been observed that the bacterial population changes with water temperature (Della Porta et al., 2021). Each hot spring locality also has slightly different dominant bacterial colonies. The bacterial assemblages found in the hot springs of Viterbo are the source of the carotenoid spectra we have studied here (Pentecost and Coletta, 2007; Della Porta et al., 2021; Valeriani et al., 2018).

2.3 Locations

Le Zitelle

The hot spring at Le Zitelle consists of three vents, ZZ and ZA as described by Folk (1994), and vent ZB (Fig. 3a). Vent ZA was not flowing at the time of this study. Vent ZZ was the main producing vent, elevated around two meters by a brick wall. The water then flows into a pool (Fig. 4a), all surrounded by a fence, before reaching a point we have named the 'Cascade' where the pool empties under the fence into the overflow channel. At sample Site 3 (Fig. 4c), the flow from vent ZB joins the main channel (Fig. 4b), leading to a confluence of the waters from the two vents.

The channel occupies a 4-metre-wide trench, which is regularly bulldozed clear of travertine deposits, and runs ESE following the Strada Valori road. The channel flows for *c*.130m from the cascade to where the water flows into a small stream. The deepest water was immediately after the cascade, *c*.30cm deep, and rarely exceeded 15cm in depth.

Patches of intermittently subaerial microbial mat characterise the proximal channel on the flanks of the channel with little colonisation of the channel centre, where the water flow is more turbulent (Fig. 4b). The microbial mats consisted of light green to yellow patches, in places covered by paper-thin rafts of carbonate. Calcified and non-calcified bubbles are also found along the sides of the proximal channel, with bubbles appearing from small, <1mm, orifices in the precipitated carbonate. In the confluence where water from vent ZB joins the water flowing from vent ZZ there are more microbial mats than in the portion of the overflow channel upstream of the confluence (Fig. 4c). Filamentous bacteria (streamers) have colonized the very edges of the flowing water, between the main water stream and the sub-arial bacterial mats. Moving distally from the confluence, the channel is heavily colonized by bacterial mats along the flanks of the channel, with the centre of the channel, where the fastest flowing and deepest water is, clear of microbial colonisation (Fig. 4d). At the distal end of the channel, the microbial assemblage is dominated by filamentous dark green bacterial bundles with varying states of calcification (Fig. 4e). The precipitation rate of the carbonate was measured over 24 hours in the proximal channel *c*.2.0m from the cascade and showed a precipitation rate of 2-4mm per day (Fig. 4f).

Bullicame

Bullicame is a shield-type travertine mound with a total diameter of *c*.250m. The central vent is within a pool *c*.10m in diameter, the water then flows down an artificial channel *c*.75m, into two pools (Fig. 3b). A safety barrier surrounds the vent and vent pool (Fig. 5a). The overflow channel is only accessible *c*.10m from the vent (Fig. 5c). The water level throughout the overflow channel was *c*.0.15m deep. The proximal channel at the first sample site at Bulicame, 5m from the safety barrier, was *c*.0.5m wide with a thin layer of bright green colouration, the green colour penetrating no more than 2-3cm into the travertine carbonate precipitate (Fig. 5c). This bright green layer is covered with a patchy layer of dark green to orange filamentous bacterial growth. In the distal parts of the channel, it narrows to *c*.0.3m wide and the bottom of the channel is fully colonized by dark green bacteria (Fig. 5d). Fossil Holocene travertines surround the vent and show calcified filamentous bacteria. Precipitation rates are estimated to be in the millimetres-per-month to millimetres-per-year.

Paliano

The vent at Paliano is a borehole drilled into the hot water aquifer. Pipes and trenched streams guide the water from this vent into a series of man-made concrete-lined pools (Fig. 3c). Water enters the first pool through a 0.15m diameter flexible pipe. The bacterial colonisation is highest in the first, hottest pool, and gradually reduces as the waters become cooler. In Pool 1 (Fig. 6a), where the water first exits the vent, the entirety of the floor of the pool is covered by a dark green to dark yellow filamentous microbial mat *c*.2cm thick, which is underlain by another *c*.2cm layer of a bright green microbial colony that penetrated the white precipitated carbonate which forms the base of the active microbial zone. (Fig. 6a, 6b). Gas bubbles have caused rafting of large areas of microbial mat, where up to a 1.0m^2 area of microbial mat breaks free of the bottom of the pool due to the buoyancy of the bubbles and floats on the surface of the pool (Fig. 3b). Moving downstream from the vent, bacterial colonisation decreased with a thin green-yellow microbial mat present at sample site 2 (Fig. 3c) and some dark green filamentous bacterial mats at sample site 3. Sample site 4 lacked microbial mats and only hosted dispersed microbial organisms. As this is a spa development site, some of the pools had been cut off from the water supply and/or were regularly cleaned, so these were not sampled. Precipitation rates are estimated to be in the millimetres-per-month to millimetres-per-year.

3. Methodology

3.1 Sample Collection

Samples were collected based on changes in the water temperature in the overflow channel, between the 15th of February and the 16th of February 2020.

A geological hammer was used to remove the samples from the hot water and each sample was immediately put into a sealed plastic sample bag and labelled with sample number, distance from the vent, and the measured water temperature at the spot the sample was removed from. Twelve samples were taken from Le Zitelle, five from Bullicame, and four samples from Paliano (see Figure 3 for sample locations). Once the samples were back in the lab, there was no preparation before the Raman spectroscopy, excepting that the dry samples were cut down using a hammer and scalpel to fit inside the laser enclosure.

3.2 Water Temperature Measurements

The water temperature at each site was measured along the transect, noted using a handheld digital thermometer (Fig. 5c).

3.3 Raman Spectroscopy

A Renishaw inVia Raman spectrometer was used to perform the Raman measurements at the University of Aberdeen. A 514.5nm diode laser, focused by a Lecia DMLM reflected light microscope to a spot of *c.* 1-2µm, was used to perform three acquisitions, each of ten seconds per datum point, at <3mW laser power at the sample. The acquisition time and laser power for this study were ascertained through a programme of pre-study test acquisitions. Sample burning was observed in some samples at higher laser powers and longer acquisition times. The Raman data were collected between 500 and 1700cm^{-1}. Each of the gross samples had ten to fifteen data points measured. The Raman spectra were processed using the Renishaw WiRE 3.0 curve-fit software. Smoothing and baseline extraction, including cubic-spline interpolation, was applied to each measurement. No deconvolution was applied to the data. A visual interpretation of the spectra was performed, identifying major peak positions and peak areas. Using Raman spectroscopy, the intensity of each peak is relative to others within the same measurement and can vary between Raman spectroscopy suites, influenced by several variables such as laser output stability and optical system used.

A literature review was performed to define the peak positions of interest: the G (graphitic) band (*c.*1585cm^{-1}) and D (disordered) band (*c.*1350cm^{-1}) of carbon, the v_1(C=C) (*c.*1515cm^{-1}), v_2(C-C) (*c.*1156cm^{-1}) and d(C=CH) (*c.*1008cm^{-1}) bands of β-carotene and the calcite / aragonite bands of 1086cm^{-1} and 712/704cm^{-1} (Cavalazzi & Westall, 2019; De Gelder et al., 2007; Edwards et al., 2011; Ellery et al., 2004; Hooijschuur et al., 2016; Lahfid et al., 2010; Muirhead et al., 2012; Sadezky et al., 2005).

Carbon has two strong Raman bands (spectral peaks), one at *c.*1585cm^{-1} the G or graphitic carbon peak, and the other at *c.*1350cm^{-1} the D or disordered carbon peak. These two bands are directly related to the physical properties of the carbon bonds, reflecting the ratio of sp^2 to sp^3 carbon bonds (Muirhead et al., 2017). The G peak (*c.*1585cm^{-1}) is a composite of the D2 (*c.*1615cm^{-1}), G (*c.*1598cm^{-1}), and D3 (*c.*1545cm^{-1}) bands, and the D peak is a combination of the D1 (*c.*1350cm^{-1}) and D4 (*c.*1200cm^{-1}) bands (Lahfid et al., 2010; Muirhead et al., 2012; Sadezky et al., 2005), these minor bands were not deconvolved. The combined D and G peaks were used for the analysis in this study.

Carotenoids display three main Raman bands, with peak positions of the common carotenoid β-carotene of *c.*1515 cm^{-1} and *c.*1156 cm^{-1} relating to in-phase stretching vibrations in the polyene chain, v_1(C=C) and v_2(C-C) respectively. The band at *c.*1008 cm^{-1} relates to CH_3 groups in-plane rocking modes, d(C=CH) (Vítek et al., 2009; Marshall and Marshall, 2010; Jehlička and Oren, 2013; Jehlička et al., 2014; Timlin et al., 2017). Timlin et al. (2017) presented several individual carotenoid spectra with individual v_1 peak positions of Lutein (1523 cm^{-1}), Echinenone (1522 cm^{-1}), Zeaxanthin (1521 cm^{-1}), β-carotene (1519 cm^{-1}), Astaxanthin (1516 cm^{-1}), and Myxoxanthophyll (1510 cm^{-1}). Jehlička et al. (2014) performed similar experiments on the cultured bacterium and found that different carotenoid peaks vary across different carotenoids. This was based on laboratory prepared carotenoid samples and may not be reflected in real-world samples.

A peak indicative of a calcite carbonate polymorph (calcite and/or aragonite) was also identified, with the primary peak position for both calcite and aragonite being 1086cm^{-1}. The main differentiator between aragonite and calcite in Raman spectra is that there are peaks at 712cm^{-1} and 282cm^{-1} for calcite, compared with 704cm^{-1} and 208cm^{-1} for aragonite (Edwards et al., 2011). While we did analyze peaks down to 500cm^{-1}, the detailed analysis of the calcite or aragonite peak was not critical to this organic carbon-focussed study and has thus been left as an undifferentiated peak. See Figure 7 for example spectra.

4. Results

4.1 Water Temperature

The temperature profiles produced from readings at the sample sites can be seen in Figure 8a. Le Zitelle had a water temperature high of 57.7°C and a low of 35.4°C. The temperature curve in Figure 8a, for Le Zitelle, has a slight upwards trend at 20m due to the confluence of the ZZ and ZB overflow channels. This location is found labelled as 'confluence' in figure 3a. The waters coming from the ZB vent were at a higher temperature (57.7°C) than the ZZ vent waters at this confluence (~53°C). There is a sharp drop off in temperature in the distal regions of the overflow channel, *c.*90m from the vent (Fig. 3a. Sample locations 10 and 11), with water depth there rarely exceeding 10 mm during the four hours of sampling at Le Zitelle and flowing at a much lower rate than at the top of the channel. In addition to the spot temperature measurements (Fig. 8a), a temperature logger was left in the pool of the Le Zitelle thermal spring, at sample site 12 (Fig. 3a), for 24 hours (Fig. 8b). A steady temperature can be seen from 14:00 on the 15th of February to 08:00 on the 16th of February, at 08:00 the temperature increased to 68°C for several hours, peaking around midday on the 16th before beginning to cool again. Spot temperature measurements of sample site 12, the closest to the vent opening, in April of 2021, gave steady temperatures of 54°C for every measurement, even over the period where the temperature was unusually high in the earlier 24-hour log.

The hot spring at Bullicame had the shortest overflow channel (*c.*70 m from vent to pools) of the three sites studied, and had the smallest change in water temperature of the three localities, with a high of 46.8°C and a low of 43.7°C. The temperature readings and samples were all taken from the overflow channel and not from the pools at the end of the channels. Sample site 3 (Fig. 3b.) shows an anomalous increase in temperature of 0.3°C compared to the next upstream measurement at sample site 2.

The waters at Paliano reached the lowest temperatures we studied around Viterbo, with a high of 46.4°C and a low of 25.0°C. The Paliano site was constructed so that the hot water sits in each of a series of pools before slowly flowing onward. This gives the water time to cool as it flows through the system.

4.2 Raman Data

Both carbon and carotenoid Raman spectra were identified in samples taken from all three sample localities. A representative selection of gathered spectra is presented in tables 1, 2 and

3, with the carotenoid peak positions. The following general observations can be made from the Raman data; The carbon spectra have more clearly defined D and G peaks as the temperature increases (Tables 1, 2 and 3). The carotenoid peaks change in intensity (relative to other carotenoid spectra in this study) and peak position (when compared to the reference peak positions from the literature review) (Table 1, 2 and 3). The relative intensity of the carotenoid peaks (relative to other carotenoid spectra in this study) increase with maturity (Fig. 10). The carotenoid spectra were partly obscured by the carbon spectrum (Fig. 10). The degree of this carbon overprinting is variable (Fig. 9). The full spread of spectral profiles, from only a carbon spectrum, through various mixed carbon and carotenoid spectra to only a carotenoid spectrum, is present in most sample sites (Fig. 9).

5. Discussion

5.1 Alteration of Carotenoid spectra

The observed carotenoid Raman spectra of the Viterbo samples are highly variable in intensity, and to a lesser degree peak position, compared to previous studies using laboratory cultured carotenoid samples (Vítek et al., 2009; Jehlička et al., 2014; Timlin et al., 2017). This change is assumed to be a function of water temperature and the bacterium's life cycle (whether the microbial assemblage is in the Lag, Exponential, Stationary or Death phase (Bruslind, 2021; Wang and Levin, 2009)). Within each sample, we also see variations between each spectrum, containing pure carbon, pure carotenoid and a range of transitional spectra that can be seen in figure 9, all taken from sample BUL-1-1, sampled at 46.8°C at the Bullicame locality. This maturation of the organic matter is shown in figure 10, where low-intensity carotenoid spectra are interpreted as 'immature' and the pure carbon spectra as 'fully mature', with a range of maturity between these points. Complicating the situation is the presence of multiple maturity levels in a single sample, meaning several different spectrum intensities are measured within each sample. This variation in maturity may be due to differing bacterial life-stages and degradation within the microbial assemblage (Bruslind, 2021; Wang and Levin, 2009). It may be due to washdown from a point upstream in the channel (at a higher temperature) which is then transported into a downstream, cooler thermal regime, where they now give an anomalously high relative intensity Raman spectrum when analyzed.

As seen in Figures 5c and 5d, the living bacterial assemblage only penetrates 5 to 6 cm into the underlying travertine deposit, meaning that under this depth we should see the gradual shift towards predominantly carbon spectra, until eventually the carotenoid spectrum is lost within the carbon spectrum.

Thus, there are two possible mechanisms of what we will refer to as 'spectral overprinting';

1. Through the bacterial assemblage dying and carbonising while at the surface as the organic matter decays.

2. Where the travertine deposit buries the bacteria, causing them to be starved of nutrients and die in a subsurface environment, where the organic matter transition to carbon has less surface condition influence.

5.2 Carbon spectra alteration with temperature

The carbon spectrum can be clearly seen at the very low geological temperatures studied here (57.7-25°C). From the data collected, it is possible to characterise the formation of the carbon spectra at low temperatures, and to explore how the carbon spectrum interacts with and is convoluted with the carotenoid spectrum. Deconvolution of the carbon spectrum from the carotenoid spectrum may be impossible at higher maturities as the stronger carbon spectrum completely covers the carotenoid spectrum.

5.3 Le Zitelle water temperature

The increased water temperature, seen in the Le Zitelle 24 hour temperature log (fig 7b.), can be attributed to influences on the pressure of the hot water reservoir. It is hypothesized that the increase in temperature seen in the 24-hour log is due to an increase in reservoir pressure due to decreased anthropogenic demand on the water supply, causing a higher flow rate at the natural vents at Le Zitelle and so allowing the water less time to cool as it rose to the surface, resulting in a higher temperature. However, as noted above, the temperature of 54°C was stable at the vent many months after the initial readings were taken.

5.4 Implications for astrobiology

The impact these findings have on Astrobiology are:

- The carotenoid and carbon spectra found in bacterial assemblages have a transitional regime as the carbon spectrum becomes dominant upon the molecular reorganisation of the carbon within the sample.
- Due to the carbon 'spectral overprinting', these biogenic carotenoid signatures may be hidden within carbon spectra, and a detailed study of the interaction and transition of carotenoid and carbon Raman spectra may open opportunities to identify biogenic carbon over abiogenic carbon positively.

- This study sets a precedent for geologically stable Raman spectral data loss due to overprinting.
- This research expands that Raman spectral library when considering carotenoid detection on Mars, supporting current and future experiments on Earth, Mars and further afield, adding insights into the preservation and detection of carotenoid compounds, while considering the complications that may be seen in convoluted spectral measurements of preserved organic matter made on Mars.

5.5 Challenges and assumptions

It is most likely that the carotenoid seen in this study is β-carotene, but without explicit confirmation, it will be referred to generally as a carotenoid. The samples were not spatially referenced when taken, with many being undifferentiated powders when the Raman spectra were taken, so they did not allow for depth-related trends to be identified. A high level of fluorescence obscures the elastic scattering response.

6. Conclusions

The key finding of this study are:

Raman spectra show a transitional regime as microbial organic material progressively degrades. Proof of biogenic origin, in the form of carotenoid compound biomarkers, might be obscured, or lost, within the Raman spectrum of carbon due to spectral overprinting. Additionally, this research expands the Raman spectral library when considering carotenoid detection for current and future planetary geology missions and considers the possible complications of convoluted spectral measurements of preserved organic matter made on Mars by the Perseverance rover (NASA) and the Rosalind Franklin rover (ESA).

Authors' Contributions

O'Donnell: Conceptualisation, Fieldwork, Investigation, Methodology, Visualisation, Writing – Original Draft.

Muirhead: Supervision, Conceptualisation, Writing – Review & Editing.

Brasier: Supervision, Conceptualisation, Writing – Review & Editing.

Capezzuoli: Fieldwork.

Acknowledgements

This study was carried out as part of a University of Aberdeen PhD, supported by the UKRI Centre for Doctoral Training in Oil & Gas. We must thank Professor Javier Martín-Torres for his valuable Martian insights, and Sig. Domenico Belli for allowing access to the Paliano spring locale, and Dr. Vereno Bisegna and Dr. Giuseppe Pagano for logistic and local assistance.

Declaration

The authors declare that they have no conflict of interest

References

Allen CC, Albert FG, Chafetz HS, et al. Microscopic Physical Biomarkers in Carbonate Hot Springs: Implications in the Search for Life on Mars. Icarus 2000;147(1):49–67; doi: 10.1006/icar.2000.6435.

Baqué M, Hanke F, Böttger U, et al. Protection of Cyanobacterial Carotenoids' Raman Signatures by Martian Mineral Analogues after High-Dose Gamma Irradiation. J Raman Spectrosc 2018;49(10):1617–1627; doi: 10.1002/jrs.5449.

Baqué M, Napoli A, Fagliarone C, et al. Carotenoid Raman Signatures Are Better Preserved in Dried Cells of the Desert Cyanobacterium Chroococcidiopsis than in Hydrated Counterparts after High-Dose Gamma Irradiation. Life 2020;10(6):1–13; doi: 10.3390/life10060083.

Beyssac O, Goffé B, Chopin C, et al. Raman Spectra of Carbonaceous Material in Metasediments: A New Geothermometer. J Metamorph Geol 2002;20(9):859–871; doi: 10.1046/j.1525-1314.2002.00408.x.

Bowden SA and Taylor CW. The Application of Surface Enhanced Raman Scattering to the Detection of Asphaltic Petroleum in Sediment Extracts: Deconvolving Three Component-Mixtures Using Look-up Tables of Entire Surface Enhanced Raman Spectra. Anal Methods 2019;11(46):5846–5856; doi: 10.1039/c9ay01859j.

Brocks JJ, Love GD, Summons RE, et al. Biomarker Evidence for Green and Purple Sulphur Bacteria in a Stratified Palaeoproterozoic Sea. Nature 2005;437(7060):866–870; doi: 10.1038/nature04068.

Brolly C, Parnell J and Bowden S. Raman Spectroscopy: Caution When Interpreting Organic Carbon from Oxidising Environments. Planet Space Sci 2016;121:53–59; doi: 10.1016/j.pss.2015.12.008.

Bruslind L. 9: Microbial Growth. In: Microbiology LibreTexts; 2021.

Busemann H, Alexander CMOD and Nittler LR. Characterization of Insoluble Organic

Matter in Primitive Meteorites by MicroRaman Spectroscopy. Meteorit Planet Sci 2007;42(7–8):1387–1416; doi: 10.1111/j.1945-5100.2007.tb00581.x.

Cartigny P, Palot M, Thomassot E, et al. Diamond Formation: A Stable Isotope Perspective. Annu Rev Earth Planet Sci 2014;42:699–732; doi: 10.1146/annurev-earth-042711-105259.

Cavalazzi B and Westall F. Biosignatures for Astrobiology. 2019.; doi: 10.1007/s11084-015-9459-9.

Chu J. A Novel Interpretation of Raman Spectra Will Help the 2020 Mars Rover Select Rocks to Study for Signs of Life. MIT News 2016.

Edwards HGM, Hutchinson IB, Ingley R, et al. The Search for Signatures of Early Life on Mars: Raman Spectroscopy and the Exomars Mission. Spectrosc Eur 2011;23(1):6–15.

Ellery A, Wynn-Williams D, Parnell J, et al. The Role of Raman Spectroscopy as an Astrobiological Tool in the Exploration of Mars. J Raman Spectrosc 2004;35(6):441–457; doi: 10.1002/jrs.1189.

Ferralis N, Matys ED, Knoll AH, et al. Rapid, Direct and Non-Destructive Assessment of Fossil Organic Matter via MicroRaman Spectroscopy. Carbon N Y 2016;108:440–449; doi: 10.1016/j.carbon.2016.07.039.

Ferrari AC and Robertson J. Resonant Raman Spectroscopy of Disordered, Amorphous, and Diamondlike Carbon. Phys Rev B - Condens Matter Mater Phys 2001;64(7):1–13; doi: 10.1103/PhysRevB.64.075414.

Folk RL. SEM Imaging of Bacteria and Nannobacteria in Carbonate Sediments and Rocks. J Sediment Petrol 1993;63(5):990–999; doi: 10.1306/d4267c67-2b26-11d7-8648000102c1865d.

Folk RL. Interaction Between Bacteria, Nannobacteria, and Mineral Precipitation in Hot Springs of Central Italy. 1994; doi: https://doi.org/10.7202/033005ar.

French KL, Rocher D, Zumberge JE, et al. Assessing the Distribution of Sedimentary C40 Carotenoids through Time. Geobiology 2015;13(2):139–151; doi: 10.1111/gbi.12126.

De Gelder J, De Gussem K, Vandenabeele P, et al. Recent Advances in Linear and Nonlinear Raman Spectroscopy I. J Raman Spectrosc 2007;38(April):1538–1553; doi: 10.1002/jrs.

Hays LE, Graham H V., Des Marais DJ, et al. Biosignature Preservation and Detection in Mars Analog Environments. Astrobiology 2017;17(4):363–400; doi: 10.1089/ast.2016.1627.

Hooijschuur JH, Verkaaik MFC, Davies GR, et al. Will Raman Meet Bacteria on Mars? An Overview of the Optimal Raman Spectroscopic Techniques for Carotenoid Biomarkers Detection on Mineral Backgrounds. Geol en Mijnbouw/Netherlands J Geosci 2016;95(2):141–151; doi: 10.1017/njg.2015.3.

Hutchinson IB, Ingley R, Edwards HGM, et al. Raman Spectroscopy on Mars: Identification of Geological and Bio-Geological Signatures in Martian Analogues Using Miniaturised Raman Spectrometers. Philos Trans R Soc A Math Phys Eng Sci 2014;372(2030); doi: 10.1098/rsta.2014.0204.

Jehlička J, Edwards HGM, Osterrothová K, et al. Potential and Limits of Raman Spectroscopy for Carotenoid Detection in Microorganisms: Implications for Astrobiology. Philos Trans R Soc A Math Phys Eng Sci 2014a;372(2030); doi: 10.1098/rsta.2014.0199.

Jehlička J and Oren A. Raman Spectroscopy in Halophile Research. Front Microbiol 2013;4(DEC):1–7; doi: 10.3389/fmicb.2013.00380.

Jehlička J, Osterrothová K, Nedbalová L, et al. Discrimination of Pigments of Microalgae, Bacteria and Yeasts Using Lightweight Handheld Raman Spectrometers: Prospects for Astrobiology. 11th Int GeoRaman Conf 2014b; doi: 10.1002/jrs.4783.

Kelemen SR and Fang HL. Maturity Trends in Raman Spectra from Kerogen and Coal. Energy and Fuels 2001;15(3):653–658; doi: 10.1021/ef0002039.

Killops S and Killops V. Introduction to Organic Geochemistry. 2nd Editio. Blackwell Publishing; 2005.

Komatsu G and Brož P. Southern Chryse Planitia on Mars As a Potential Landing Site: Investigation of Hypothesized Sedimentary Volcanism. 52nd Lunar Planet Sci Conf 2021;8(2548):122–127.

Lahfid A, Beyssac O, Deville E, et al. Evolution of the Raman Spectrum of Carbonaceous Material in Low-Grade Metasediments of the Glarus Alps (Switzerland). Terra Nov 2010;22(5):354–360; doi: 10.1111/j.1365-3121.2010.00956.x.

Lee C and Brocks JJ. Identification of Carotane Breakdown Products in the 1.64billion Year Old Barney Creek Formation, McArthur Basin, Northern Australia. Org Geochem 2011;42(4):425–430; doi: 10.1016/j.orggeochem.2011.02.006.

Leuko S, Bohmeier M, Hanke F, et al. On the Stability of Deinoxanthin Exposed to Mars Conditions during a Long-Term Space Mission and Implications for Biomarker Detection on Other Planets. Front Microbiol 2017;8(SEP):1–11; doi: 10.3389/fmicb.2017.01680.

Linares R and Rodríguez A. Tufa Mounds on Earth and Mars. 2013.

Ma J and Cui X. Aromatic Carotenoids: Biological Sources and Geological Implications. Geosystems and Geoenvironment 2022;1(2):100045; doi: 10.1016/j.geogeo.2022.100045.

Maoka T. Carotenoids as Natural Functional Pigments. J Nat Med 2020;74(1):1–16; doi: 10.1007/s11418-019-01364-x.

Des Marais DJ and Walter MR. Terrestrial Hot Spring Systems: Introduction. Astrobiology

2019;19(12):1419–1432; doi: 10.1089/ast.2018.1976.

Marshall CP and Marshall AO. The Potential of Raman Spectroscopy for the Analysis of Diagenetically Transformed Carotenoids. Philos Trans R Soc A Math Phys Eng Sci 2010;368(1922):3137–3144; doi: 10.1098/rsta.2010.0016.

McMahon S, Bosak T, Grotzinger JP, et al. A Field Guide to Finding Fossils on Mars. J Geophys Res Planets 2018;123(5):1012–1040; doi: 10.1029/2017JE005478.

Morris R V., Ruff SW, Gellert R, et al. Identification of Carbonate-Rich Outcrops on Mars by the Spirit Rover. Science (80-) 2010;329(5990):421–424; doi: 10.1126/science.1189667.

Muirhead DK, Bond CE, Watkins H, et al. Raman Spectroscopy: An Effective Thermal Marker in Low Temperature Carbonaceous Fold-Thrust Belts. Geol Soc London, Spec Publ 2019;SP490-2019–27; doi: 10.1144/sp490-2019-27.

Muirhead DK, Parnell J, Spinks S, et al. Characterization of Organic Matter in the Torridonian Using Raman Spectroscopy. Geol Soc Spec Publ 2017;448(1):71–80; doi: 10.1144/SP448.2.

Muirhead DK, Parnell J, Taylor C, et al. A Kinetic Model for the Thermal Evolution of Sedimentary and Meteoritic Organic Carbon Using Raman Spectroscopy. J Anal Appl Pyrolysis 2012;96:153–161; doi: 10.1016/j.jaap.2012.03.017.

Pasteris JD and Wopenka B. Necessary, but Not Sufficient: Raman Identification of Disordered Carbon as a Signature of Ancient Life. Astrobiology 2003;3(4):727–738; doi: 10.1089/153110703322736051.

Pedley MH. Tufas and Travertines. In: Sedimentology. Encyclopedia of Earth Science Springer, Berlin, Heidelberg; 1978; doi: https://doi.org/10.1007/3-540-31079-7_243.

Pentecost A and Coletta P. The Role of Photosynthesis and CO2 Evasion in Travertine Formation: A Quantitative Investigation at an Important Travertine-Depositing Hot Spring, Le Zitelle, Lazio, Italy. J Geol Soc London 2007;164(4):843–853; doi: 10.1144/0016-76492006-037.

Piscopo V, Barbieri M, Monetti V, et al. Hydrogeology of Thermal Waters in Viterbo Area, Central Italy. Hydrogeol J 2006;14(8):1508–1521; doi: 10.1007/s10040-006-0090-8.

Della Porta G, Hoppert M, Hallmann C, et al. The Influence of Microbial Mats on Travertine Precipitation in Active Hydrothermal Systems (Central Italy). Depos Rec 2021;(July); doi: 10.1002/dep2.147.

Razzell Hollis J, Abbey W, Beegle LW, et al. A Deep-Ultraviolet Raman and Fluorescence Spectral Library of 62 Minerals for the SHERLOC Instrument Onboard Mars 2020. Planet Space Sci 2021;209(August):105356; doi: 10.1016/j.pss.2021.105356.

Rodríguez JAP, Tanaka KL, Kargel JS, et al. Formation and Disruption of Aquifers in Southwestern Chryse Planitia, Mars. Icarus 2007;191(2):545–567; doi: 10.1016/j.icarus.2007.05.021.

Rouzaud JN, Oberlin A and Beny-Bassez C. Carbon Films: Structure and Microtexture (Optical and Electron Microscopy, Raman Spectroscopy). Thin Solid Films 1983;105(1):75–96; doi: 10.1016/0040-6090(83)90333-4.

Ruff SW, Campbell KA, Van Kranendonk MJ, et al. The Case for Ancient Hot Springs in Gusev Crater, Mars. Astrobiology 2020;20(4):475–499; doi: 10.1089/ast.2019.2044.

Ruff SW and Farmer JD. Silica Deposits on Mars with Features Resembling Hot Spring Biosignatures at El Tatio in Chile. Nat Commun 2016;7:1–10; doi: 10.1038/ncomms13554.

Rull F, Maurice S, Hutchinson I, et al. The Raman Laser Spectrometer for the ExoMars Rover Mission to Mars. Astrobiology 2017;17(6–7):627–654; doi: 10.1089/ast.2016.1567.

Sadezky A, Muckenhuber H, Grothe H, et al. Raman Microspectroscopy of Soot and Related Carbonaceous Materials: Spectral Analysis and Structural Information. Carbon N Y 2005;43(8):1731–1742; doi: 10.1016/j.carbon.2005.02.018.

Shirey SB and Shigley JE. Recent Advances in Understanding the Geology of Diamonds. Gems Gemol 2013;(Winter):188–222.

Sinninghe Damsté JS and Koopmans MP. The Fate of Carotenoids in Sediments: An Overview. Pure Appl Chem 1997;69(10):2067–2074; doi: 10.1351/pac199769102067.

Takaichi S and Mochimaru M. Carotenoids and Carotenogenesis in Cyanobacteria: Unique Ketocarotenoids and Carotenoid Glycosides. Cell Mol Life Sci 2007;64(19–20):2607–2619; doi: 10.1007/s00018-007-7190-z.

Timlin JA, Collins AM, Beechem TA, et al. Localizing and Quantifying Carotenoids in Intact Cells and Tissues. Carotenoids 2017;(June); doi: 10.5772/68101.

Tuinstra F and Koenig J. Raman Spectrum of Graphite. J Chem Phys 1970;53(3):1126–1130; doi: 10.1063/1.1674108.

Valeriani F, Crognale S, Protano C, et al. Metagenomic Analysis of Bacterial Community in a Travertine Depositing Hot Spring. New Microbiol 2018;41(2):126–135; doi: 10.5281/zenodo.3888416.

Vítek P, Jehlicka J, Edwards HGM, et al. Miniaturized Raman Instrumentation Detects Carotenoids in Mars-Analogue Rocks from the Mojave and Atacama Deserts. Philos Trans R Soc A Math Phys Eng Sci 2014;372(2030); doi: 10.1098/rsta.2014.0196.

Vítek P, Osterrothová K and Jehlička J. Beta-Carotene-A Possible Biomarker in the Martian Evaporitic Environment: Raman Micro-Spectroscopic Study. Planet Space Sci

2009;57(4):454–459; doi: 10.1016/j.pss.2008.06.001.
Wang JD and Levin PA. Metabolism, Cell Growth and the Bacterial Cell Cycle. Nat Rev Microbiol 2009;7(11):822–827; doi: 10.1038/nrmicro2202.
Wopenka B. Raman Observations on Individual Interplanetary Dust Particles. Earth Planet Sci Lett 1988;88(3–4):221–231; doi: 10.1016/0012-821X(88)90079-9.
Wopenka B and Pasteris JD. Structural Characterization of Kerogens to Granulite-Facies Graphite: Applicability of Raman Microprobe Spectroscopy. Am Mineral 1993;78(5–6):533–557.

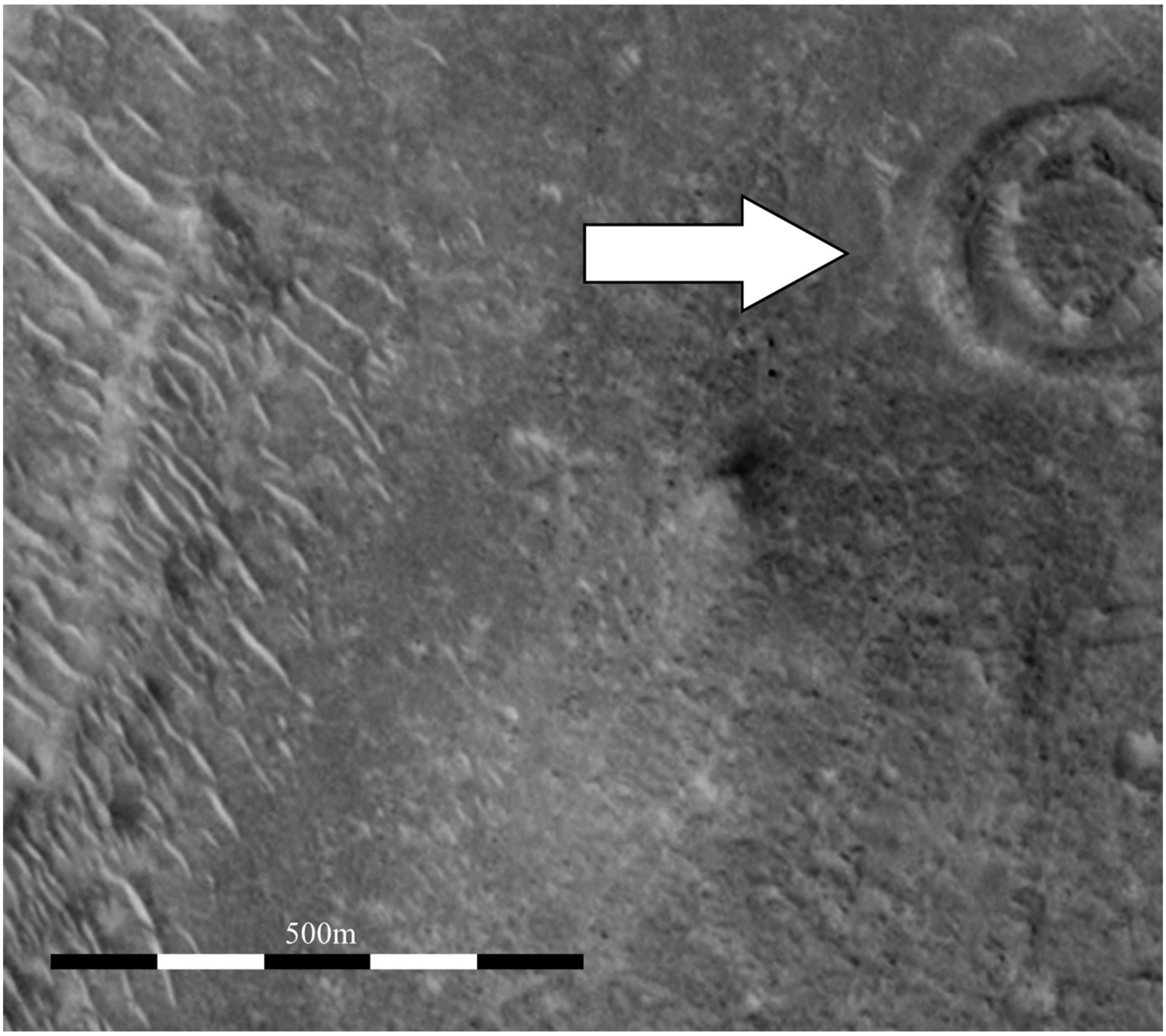

FIG. 1.

Figure 1. Part of image R09-03319 from the Mars Orbiter Camera (MOC) of an area of the Chryse Planitia, showing a circular feature hypothesised to be a tufa mound.

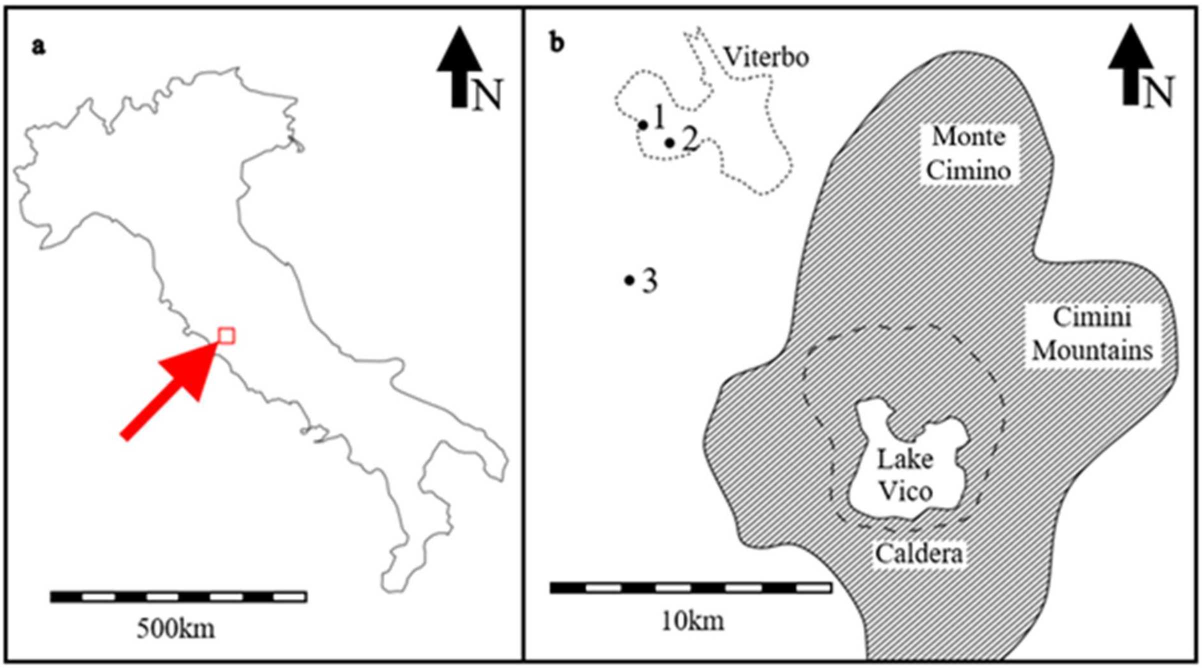

FIG. 2.

(**a**) Simplified overview of Italy and the location of the study area. (**b**) Diagrammatic map showing an outline of the city of Viterbo and the surrounding geographical features. The Cimini Mountains and Lake Vico are important sources of meteoric water that feed into the hot spring systems of Viterbo. Sample sites for this study: 1. Le Zitelle (42°25’34” N, 12°03’39” E, Elevation 291m a.s.l.), 2. Bullicame (42°25’13” N, 12°04’22” E, Elevation 297m a.s.l.), 3. Paliano (42°22’35” N, 12°03’26” E, Elevation 255m a.s.l.).

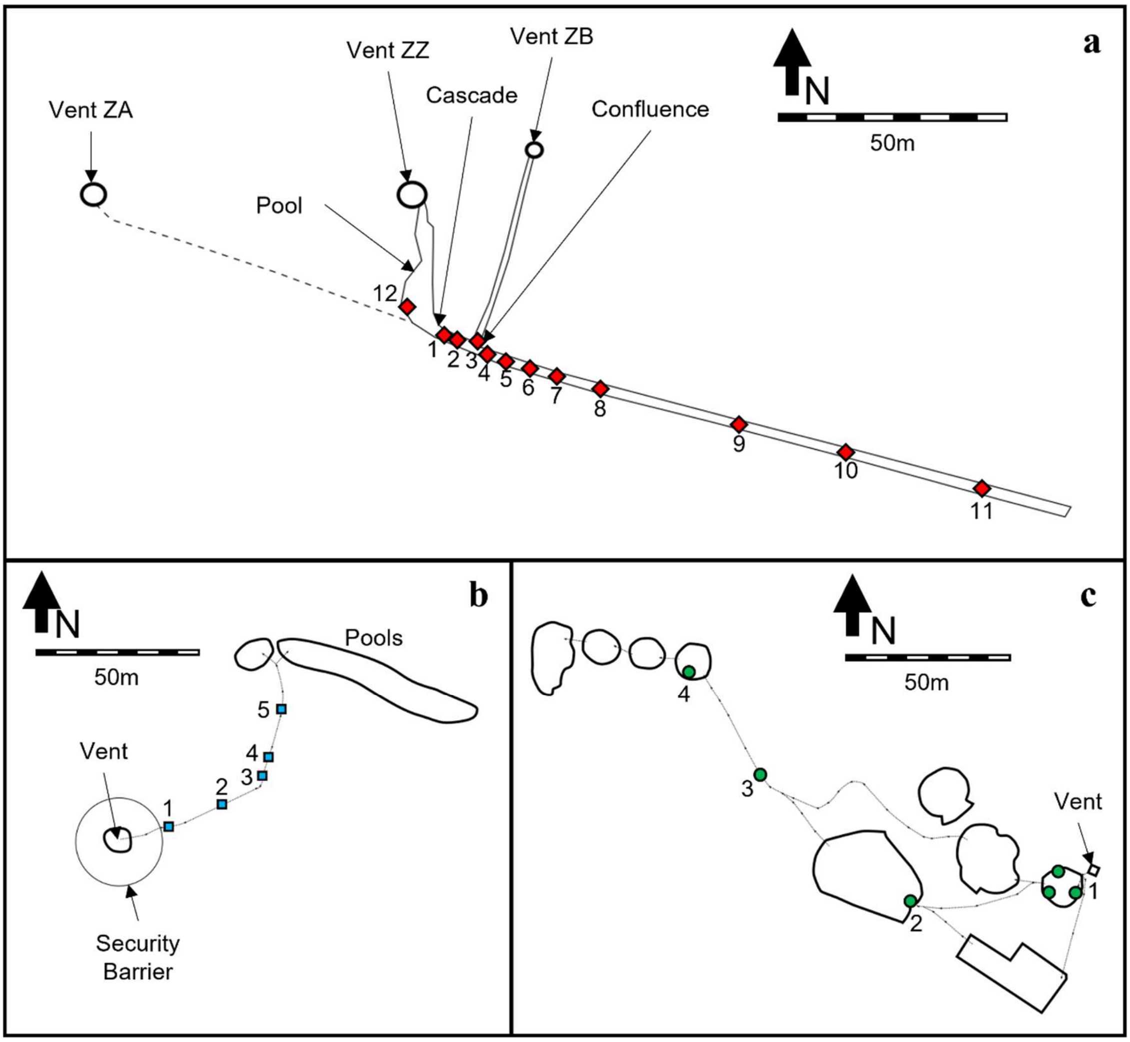

FIG. 3.

Map diagrams of each sample locality visited for this study. The numbers denote sample sites for each locality and the letters in boxes represent the photographs that can be found in Figure 4.

(**a**) – Le Zitelle (Vent ZA: 42°25’34.20”N 12°03’35.97”E; Vent ZZ: 42°25@34.21”N 12°03’38.92”E; Vent ZB: 42°25’34.50”N 12°03’40.06”E). Consisting of several vents flowing into an artificial channel that is regularly excavated due to >1mm deposition rate of carbonates. Vent ZA and ZZ were described by Folk (1994) and are surrounded by man-made brick structures, and the newer, possibly artificial, vent ZB has been labelled as such by these authors for the sake of the naming convention at this site. Vent ZA was not flowing at the time this data was collected. Vent ZZ was the main vent for this system and can be seen in photograph (a) in Figure 4.

(**b**) – Bullicame (Vent: 24°25'13.50"N 12°04'22.73"E). A shield-type hot spring vent, the deposition rate at Bullicame is quite low, and the flow rate of the vent can vary greatly due to anthropomorphic influences in the nearby area.

(**c**) – Paliano (Vent: 42°22'35.17"N 12°03'26.17"E). An artificial hot spring site, the Paliano site is a currently under construction facility using hot waters from a drilled well that flow into concrete lined pools. The deposition rate at this site is also low.

The topography at these sites does not change because the channels are artificially excavated to maintain flow.

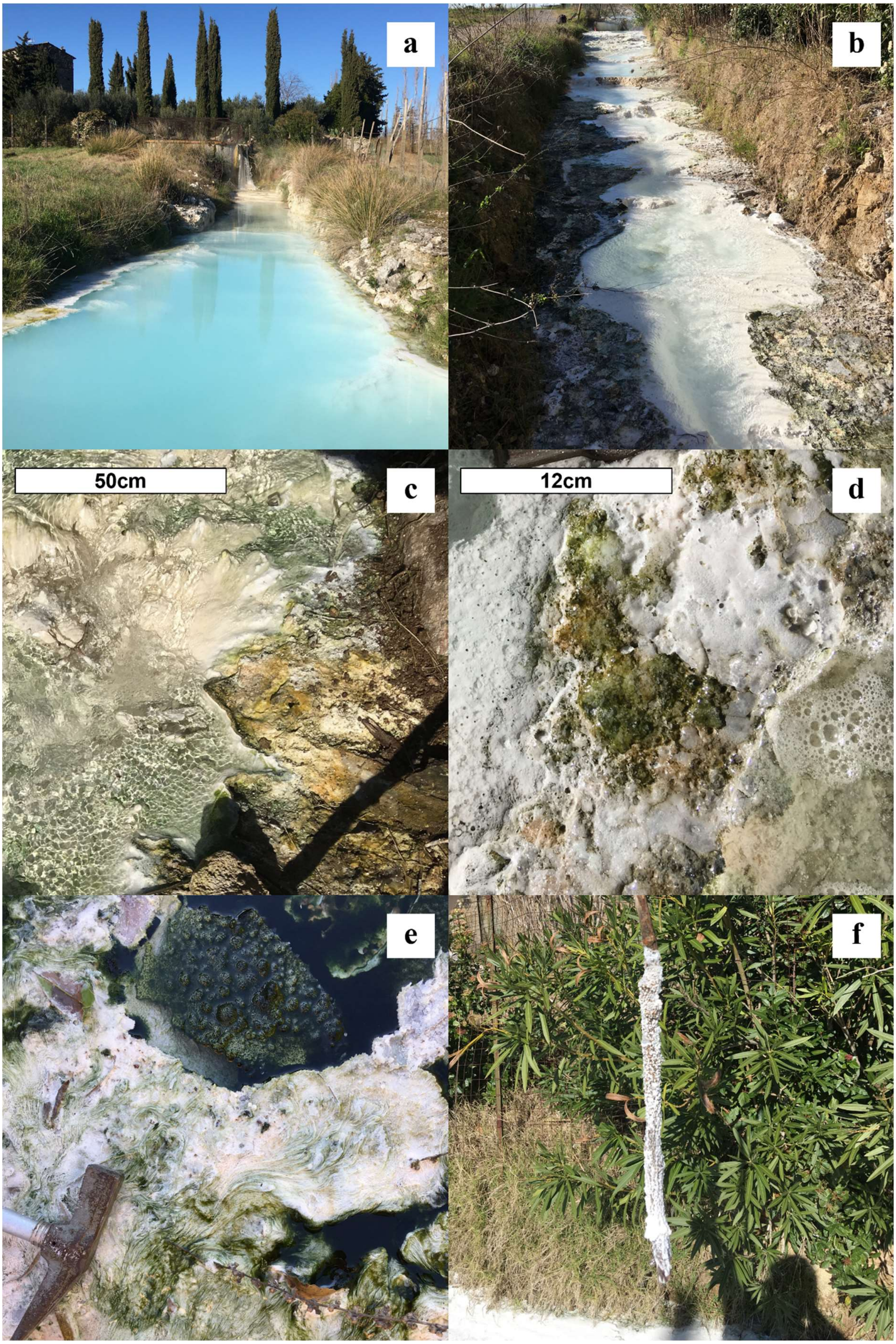

726
727

FIG. 4.

(**a**) – Vent ZZ at Le Zitelle, the pool in the foreground, is where the 24-hour temperature log was taken. The vent itself can be seen in the photo's background flowing over the enclosing brick structure, trees in background measure 15m tall.

(**b**) – A view up the overflow channel from 20m downstream of the 'cascade' showing the spatial association of the bacterial assemblages on the flanks of the channel, and the fast-flowing water, clear of organic growth in the centre of the channel. The width of the of channel is ~1.8m wide.

(**c**) – The confluence of waters from vent ZB entering the main channel at Le Zitelle. The width of the field of view is 20cm.

(**d**) – A close-up of a bacterial colony in the main channel at Zitelle. Here the main water stream is to the left of the photograph, while there is a subaerial pool facies to the right of the photograph. In these low energy pools the greatest bacterial build-up takes place in the upper channel. The width of the field of view is 1m.

(**e**) – Distal channel bacterial mats, showing filamentous bacterial growth. The head of geological hammer in frame is 15cm long.

(**f**) – A wooden stick (piece of branch) is used to measure of precipitation rate in the deepest part of the Le Zitelle overflow channel over 24 hours. Carbonate build-up of 2-4mm was observed. The stick is 1.5cm thick.

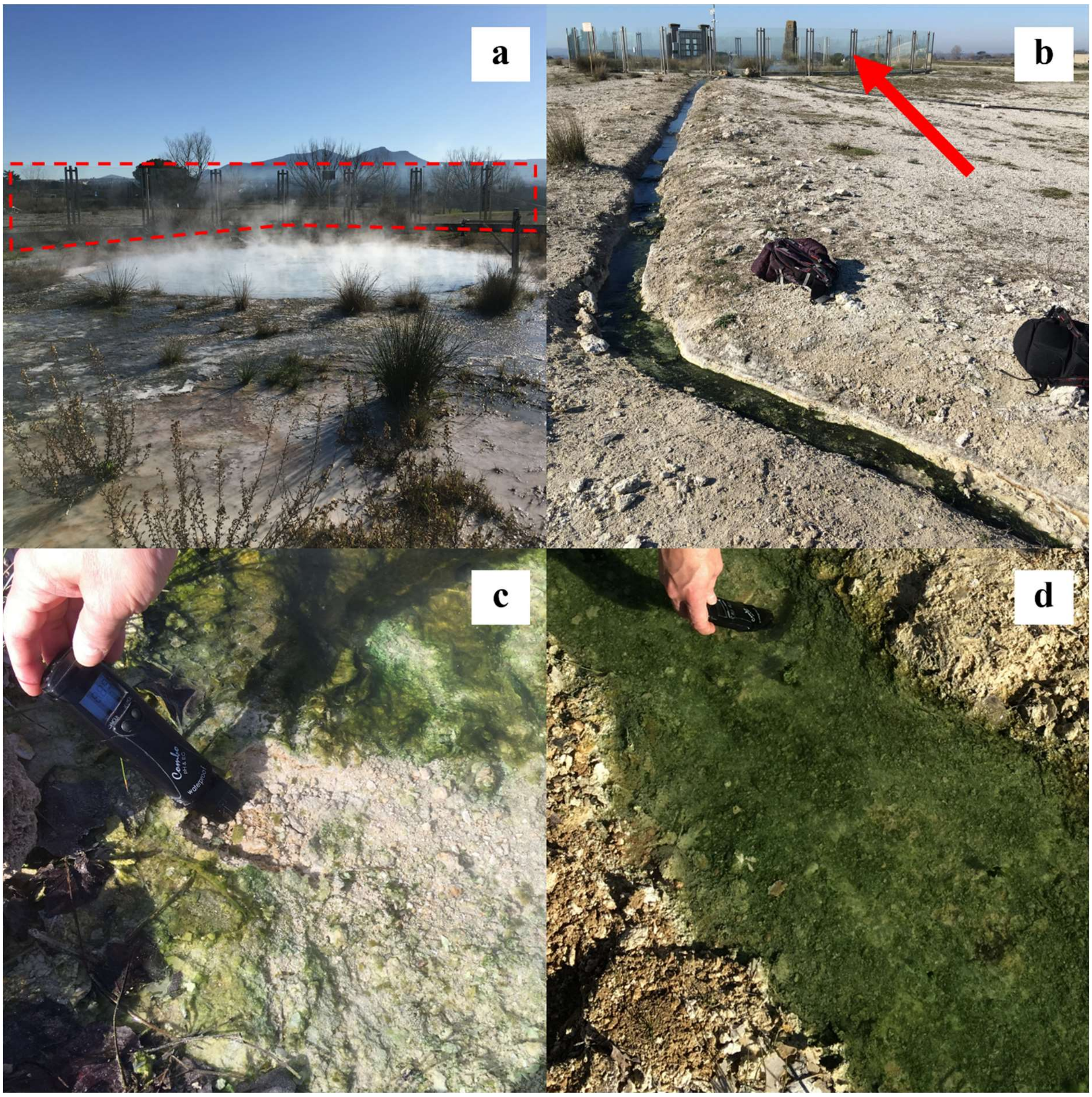

FIG. 5.

(**a**) – The vent at Bullicame is taken through a gap in the protective barrier, which is visible in the background (Support pillars and glass barrier, outlined in red). The vent pool, which is seen here steaming, is 8m in diameter.

(**b**) – The overflow channel showing the narrowness of the overflow channel compared to Le Zitelle (Fig. 4b) and Paliano (Fig. 6a). At the top of the image, the diameter of the security barrier in the background (Red arrow indicating support pillars) is 25m.

(**c**) – Taking temperature readings in the proximal channel using a handheld digital thermometer. The thin layer of bright green cyanobacteria is visible here, in places covered with a patchy layer of dark green to orange filamentous bacterial growth. The thermometer is around 15cm long.

(**d**) – Taking temperature readings in the distal channel, with dark green filamentous bacteria fully colonising the bottom of the channel. The thermometer is around 15cm long.

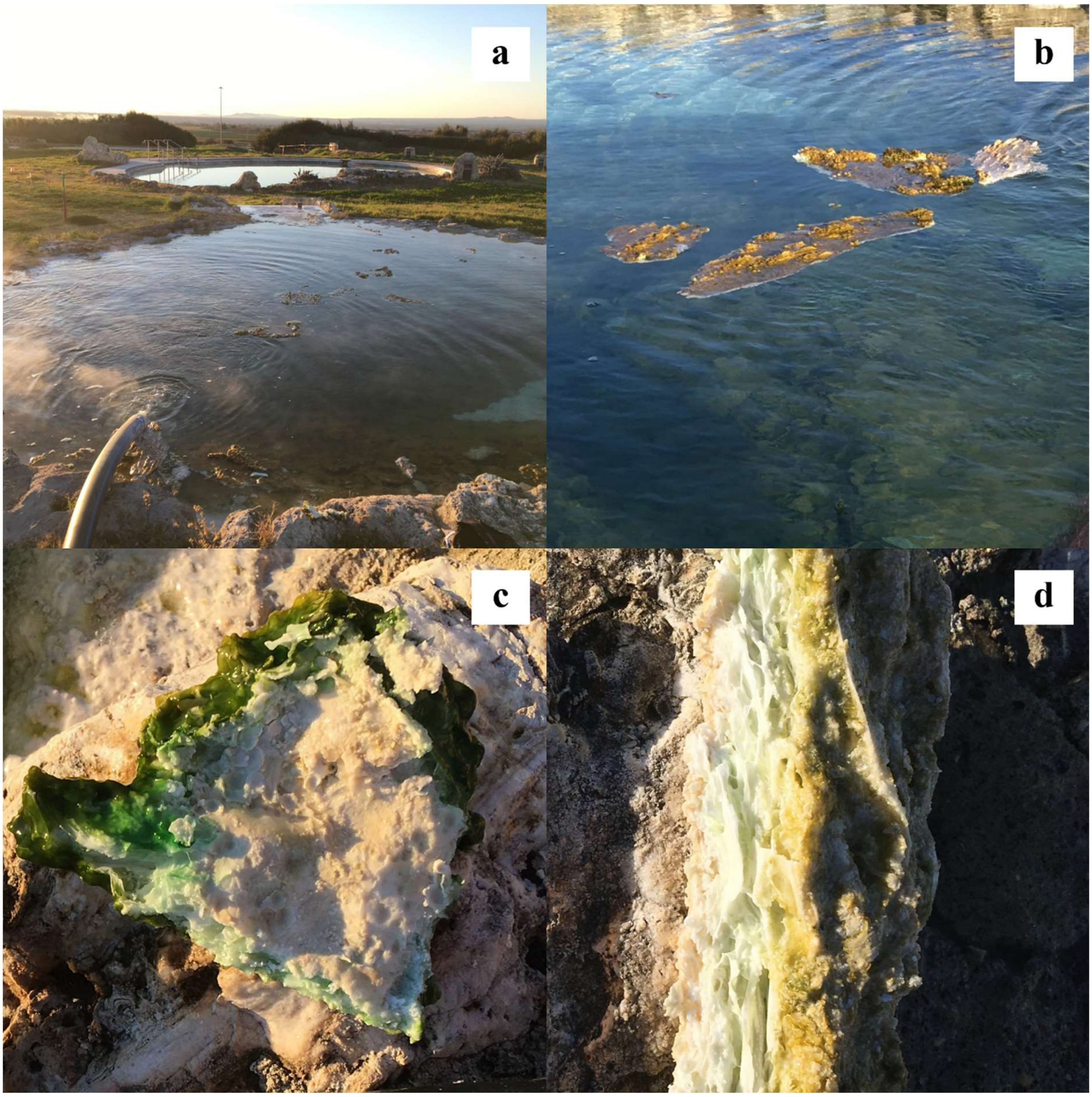

FIG. 6.

(**a**) – At the Paliano site, looking over Pool 1 (Site 1, Fig. 3c) to the north-east. The pipe from which the water first enters the pools is visible in the bottom left corner. The diameter of Pool 1 is 10.5m.

(**b**) – Rafting in Pool 1, caused by calcification of gas bubbles causing large areas of microbial mat to break free of the bottom of the pool due to the buoyancy of the bubbles and float on the surface of the water. The diameter of image is 3m.

(**c**) – Sample taken from the bottom of pool 1, at sample site 1 (Fig. 3b) at Paliano. The sample is upside down in relation to its in-situ position. The dark green to dark yellow filamentous microbial assemblage, underlain by a layer of bright green microbial colonisation is visible in an upside-down format. The sample is 16cm across.

(**d**) – Another sample was taken from the bottom of pool 1, at sample site 1 (Fig. 3b) at Paliano. The sample is on its side in relation to its in-situ position, with the right surface in contact with the water and the left edge buried within the carbonate precipitate. The same dark green to dark yellow filamentous microbial layer, and the bright green layer, is visible. Sample is 6cm from left to right.

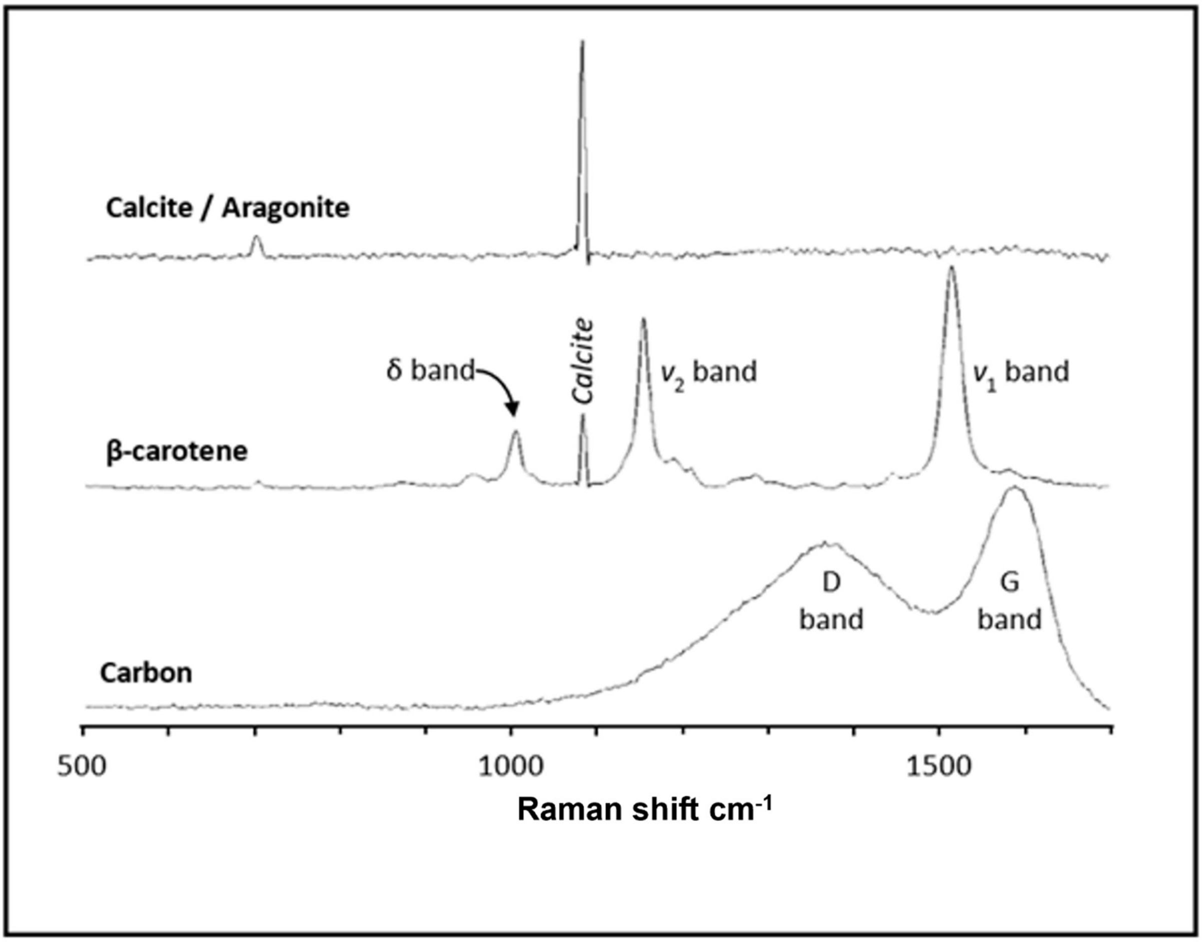

FIG 7.

Example spectra from Viterbo samples, showing the main Raman bands being investigated: the G (graphitic) band (c.1585 cm^{-1}) and D (disordered) band (c.1350cm^{-1}) of carbon, the v_1(C=C) (c.1515 cm^{-1}), v_2(C-C) (c.1156 cm^{-1}) and δ(C=CH) (c.1008 cm^{-1}) bands of β-carotene, and the calcite / aragonite bands of 1086cm-1 and 712/704cm^{-1}. The Raman measurements for this study only measured down to 500cm^{-1}, so the lower diagnostic Raman bands of the calcite/aragonite spectrum were not observed.

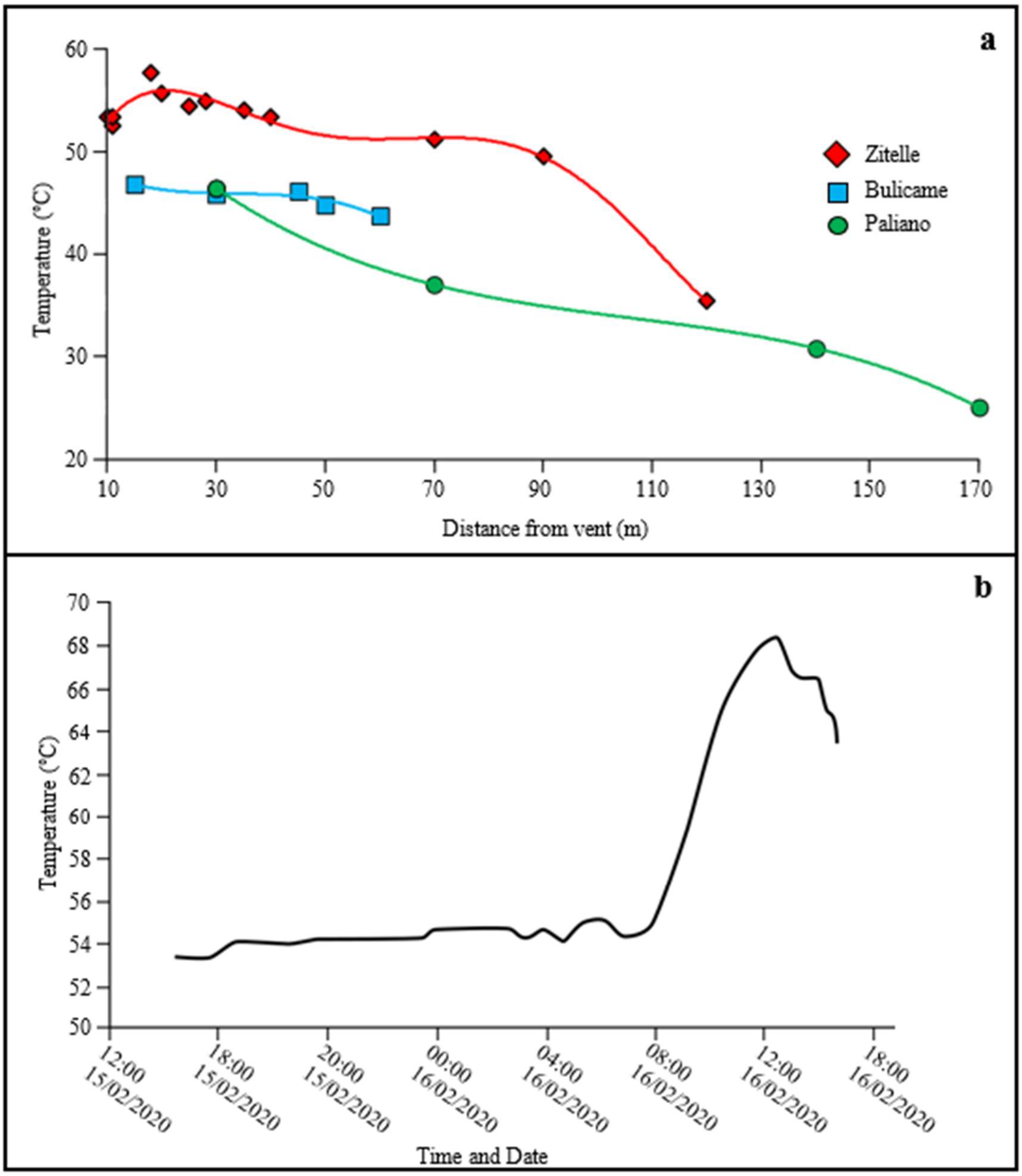

FIG. 8.

Temperature curves for (**a**) the three sample sites showing the rate the water temperature cooled in relation to distance from the vent, and (**b**) 24-hour temperature logger data from Le Zitelle that was placed at the 'number 12' sample site (see Figure 4, Images F & G). The rise in temperature at ~08:00 on the 16th, from 54°C up to 68°C and then falling again when the measurements were stopped, could be attributed to anthropomorphic activities affecting the flow rate at this site. The temperature at Zitelle was spot measured several times in May 2021 at the same location, including at the same time interval, and was found each time to be 54°C.

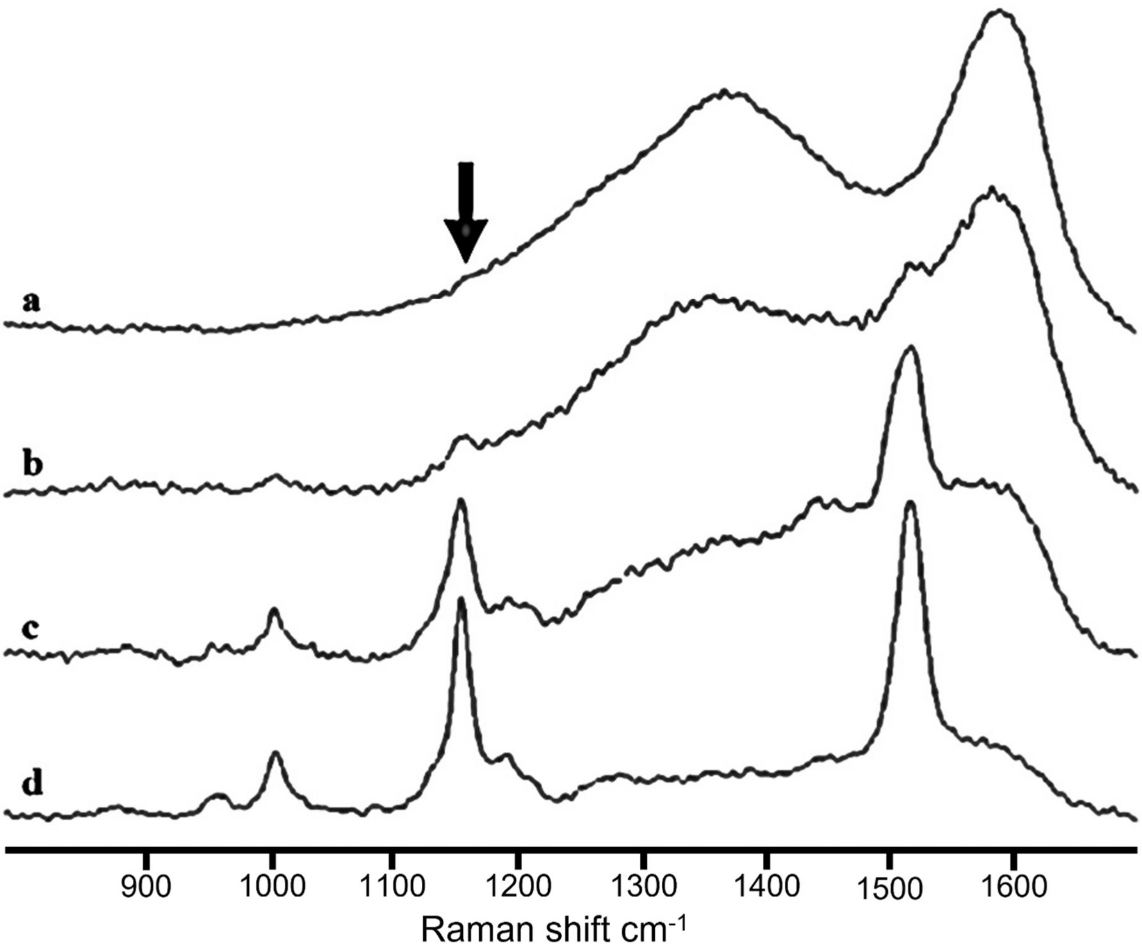

FIG. 9.

Spectra from Bullicame hot spring, sample number BUL-1-1, spatially located in figure 3b with the number 1. Each of these 4 Raman spectrums were measured from the same sample, from different areas within the same sample. They show the variety of organic maturity that can be seen in a single sample due to a difference in local thermal maturity, washdown from different thermal regimes, or from life/death changes in the bacterial mat. Referring to an idealised progression of maturity presented in figure 10, spectrum **d** shows a mid-maturity carotenoid spectrum with the beginnings of the carbon spectrum formation visible, spectrum **c** and **b** show the transition spectrum where the carbon spectra is overprinting the carotenoid spectrum, and spectrum **a** no longer shows any obvious sign of the carotenoid spectrum, except for a slight hump in the location we would expect to see the V_2 carotenoid spectral band (arrow).

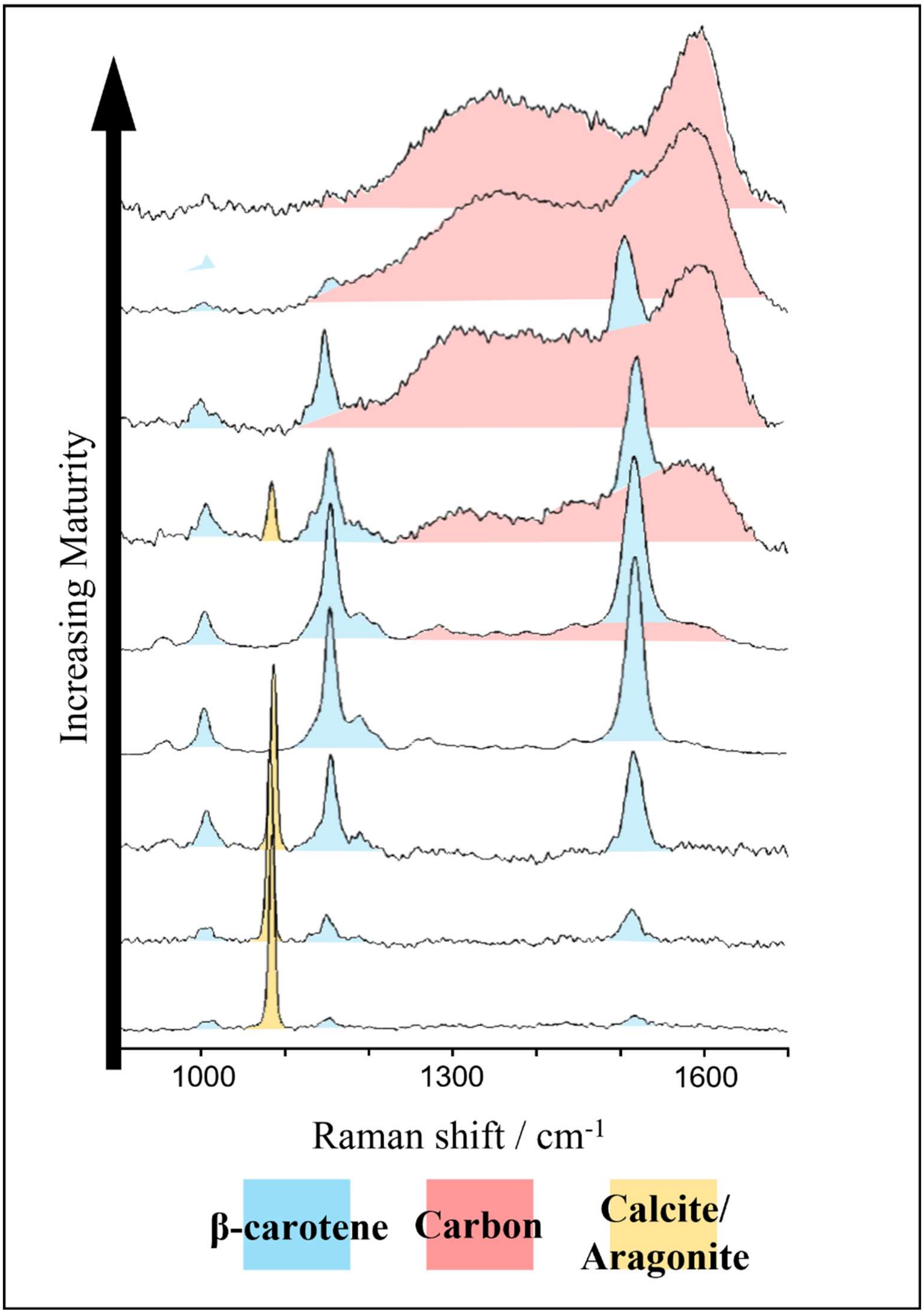

FIG. 10.

Idealised organic maturity sequence of the Raman data in this study irrespective of measured temperature. This diagram shows a very low intensity carotenoid (blue) spectrum at the lowest end of the maturity sequence, and the carotenoid spectra increase in intensity with organic maturity before the carbon (red) spectrum begins to form halfway through the sequence. The D and G peaks of the carbon spectra increase in intensity as the organic matter matures further, with the carotenoid spectral signature being subsumed by the carbon spectrum. At full maturity the Raman spectrum of the organic matter no longer shows any carotenoid signature, only presenting the carbon spectral bands.